Acta Materialia 127 (2017) 85–97

Contents lists available at ScienceDirect

Acta Materialia

journal homepage: www.elsevier.com/locate/actamat

Full length article

Dependence of dislocation structure on orientation and slip systems in highly oriented nanotwinned Cu

Qiuhong Lu [a], Zesheng You [a, b], Xiaoxu Huang [c], Niels Hansen [c], Lei Lu [a, *, 1]

[a] Shenyang National Laboratory for Materials Science, Institute of Metal Research, Chinese Academy of Sciences, Shenyang, 110016, PR China
[b] Herbert Gleiter Institute of Nanoscience, Nanjing University of Science and Technology, 200 Xiaolingwei Street, Nanjing, 210094, PR China
[c] Section for Materials Science and Advanced Characterization, Department of Wind Energy, Technical University of Denmark, Risø Campus, DK-4000, Roskilde, Denmark

ARTICLE INFO

Article history:
Received 3 September 2016
Received in revised form
12 December 2016
Accepted 8 January 2017
Available online 11 January 2017

Keywords:
Nanotwinned Cu
Slip system
Dislocation structure
TEM
Two-beam diffraction

ABSTRACT

To explore the correlation between orientation, active slip systems and dislocation structure, highly oriented nanotwinned Cu has been deformed in compression to 2% and 6% strain. The compression directions are 90°, 0° and 45° with respect to the twin boundaries (TBs) of the almost parallel twins. The dislocation structures are analyzed by the two-beam diffraction imaging in a transmission electron microscope and by a Schmid factor analysis. In structures deformed at 90° a high density of long straight dislocation lines with both slip plane and Burgers vectors inclined to the twin plane (slip Mode I) are observed; they transmit across multiple TBs at a strain of 2% and form a high density of dislocations on TBs at a strain of 6%. In structures deformed at 0° dislocations with Burgers vectors parallel to the twin plane (slip Mode II) are confined within Twin/Matrix lamellae and the analysis shows that both slip Mode I and II are active with dominance of Mode II. In structures deformed at 45° dislocations from slip Modes I, II and III are identified, where Mode III dislocations consist of partial dislocations moving along the TBs and full dislocations inside the twin lamellae gliding on the slip planes parallel to the twin plane. The analysis of the dislocation structures illustrate the strong correlation between active slip systems and the dislocation structure and the strong effect of slip mode anisotropy on both the flow stress and strain hardening rate of nanotwinned Cu.

1. Introduction

Nanotwinned (nt) metals have been studied extensively because of their novel mechanical and physical properties [1–13]. It has been shown that when a high density of twin boundaries (TBs) spaced on the nanometer scale was introduced into ultra-fine grains, the metals can be significantly strengthened while retaining considerable plasticity and work hardening [2,14]. Both experiments [15–17] and molecular dynamics (MD) simulations [18,19] have revealed that the novel mechanical properties of nt-metals originate from the interactions between dislocations and TBs. The presence of nanoscale TBs in the grains changes the dislocation glide mechanisms significantly [20,21]. Such interactions become increasingly frequent and more important in nanoscale twin lamellae which have a large density of TBs.

Studies based on MD simulations, dislocation mechanics and crystal plasticity have shown that the deformation mechanisms in face-centered cubic (fcc) nt-metals can be classified into three modes according to the dislocation activity [13]: (i) dislocation pile-up and slip transfer across TBs (Mode I); (ii) threading dislocations and confined-layer-slip (Mode II) and (iii) slip of partial dislocations along TBs (Mode III, also named Soft Mode) [13]. In addition, interactions between dislocations and TBs are complex and they depend on many parameters: type of TBs [22–25] (coherent TB (CTB) and incoherent TB (ITB)), the character of incoming dislocations (screw or non-screw dislocations) [26–28], twin thickness [18,29,30], applied/local stresses and the loading direction with respect to the TBs [31–34].

The deformation mechanisms of nt-metals have also been investigated by in-situ transmission electron microscopy (TEM) and post-mortem TEM observations. In-situ TEM observations indicate that gliding of Shockley partial dislocations from the ITBs will lead

* Corresponding author.
E-mail address: llu@imr.ac.cn (L. Lu).

[1] Professor Lei Lu was an editor of the journal during the review period of the article. To avoid a conflict of interest, Professor Irene J. Beyerlein acted as editor for this manuscript.

http://dx.doi.org/10.1016/j.actamat.2017.01.016
1359-6454/

to a rapid migration of ITBs and result in detwinning [35–38]. The process of a perfect dislocation transmission across the TBs has been clearly illustrated by in-situ TEM observations [25,39], as well as the interaction of dislocations with the TBs [40,41]. The transition from perfect dislocation nucleation and transmission across TBs to dislocation slip along and parallel to the twin plane (Soft Mode) has closely been associated with local stress variations in the twin lamellae [42].

Actually, post-mortem TEM studies of plastic deformation of nt-metals have focused on the microstructural morphology at large plastic strain, near the necking region in tensile samples [15,32]. The deformation microstructures have been characterized as a large amount of dislocation debris and different dissociated dislocations in the vicinity of TBs. Strong interactions, dislocation/dislocation and dislocation/TB make it very difficult to characterize the behavior of individual dislocations and to resolve the initiation/interaction processes behind the structural evolution.

In a columnar grained nt-Cu with preferentially oriented twins, a strong anisotropic mechanical behavior has been found [31] when loading in different directions with respect to the TBs. The anisotropic behavior of nt-Cu was analyzed by applying a plasticity model [43] identifying the active slip systems classified as the three slip Modes (I, II III) [13]. The different slip modes will lead to different paths of the microstructural evolution, which suggests an analysis of dislocations and dislocation patterns in deformed nt-Cu. This is the objective of the present study of nt-Cu deformed in different directions with respect to the almost parallel twin planes. The analysis has been done by two-beam diffraction imaging in a transmission electron microscope (TEM) to accurately characterize the Burgers vectors and the morphology of the active dislocations, to reveal the effect of orientation and slip system on the dislocation structure and the interaction of dislocations from different slip systems with TBs. Small plastic strains in compression (2% and 6%) have been applied to analyze in detail the effect of slip mode and the structure evolution. This analysis underpins a discussion of the flow stress and work hardening behavior of nt-Cu also including a Schmid factor analysis.

2. Experimental

2.1. Experimental procedures

High-purity Cu (99.99 wt%) sheets with nanoscale growth twins were synthesized by means of direct-current electro-deposition from an electrolyte of $CuSO_4$. More details about the deposition parameters were described in Ref. [31]. The nt-Cu sheet was deposited to a final thickness of more than 1.5 mm by carefully controlling the deposition parameters. The microstructure of the as-deposited Cu specimens is shown in Fig. 3 of [31]. The as-deposited sample consists of micron/submicron-sized columnar grains with {111} out-of-plane texture. The grain size is in the range from 1 to 6 μm, with an average value of about 3 μm. These columnar grains are subdivided by nanoscale twin lamellae, most of which are parallel to the deposited sheet plane. Statistical analysis shows that the average twin thickness is about 30 nm [31].

Rectangular compression samples with a cross-section area of 0.8×0.8 mm^2 and a length of 1.2 mm were cut from the deposited sheet. These samples were compressed in three directions, perpendicular, parallel and 45° to the deposition plane/twin plane, (termed 90° compression, 0° compression and 45° compression). The uniaxial compression tests were performed on an Instron 5848 micro tester with a 2 kN load cell at a strain rate of 1×10^{-3} s^{-1} at room temperature. The plastic strain measured from the height reduction of compressed samples was 2% and 6%. To minimize the friction between samples and platens, vaseline was used as a lubricant during the compression tests.

TEM observations of dislocation structures in the deformed samples were mainly conducted in a cross-section parallel to the compression axis. However, for the 0° compression sample a cross section 45° to the compression axis has also been analyzed (see Section 3). TEM foil samples were prepared by mechanical polishing followed by twin-jet electro-polishing in an electrolyte of phosphoric acid (25%), alcohol (25%) and deionized water (50%) at −10 °C. The TEM foils were examined in a JEOL 2010 electron microscope operating at 200 kV and a Tecnai F20 electron microscope operating at 200 kV.

2.2. Analysis of slip modes and determination of Burgers vectors

To illustrate the slip systems in the nt-Cu sample, a pair of Thompson tetrahedra corresponding to the matrix and twinned crystals is shown in Fig. 1. There are 12 equivalent {111}<110> slip systems in either the matrix or the twin; the 12 slip systems for the matrix are listed in Table 1. As the three slip systems associated with the twin plane are shared by the matrix and the twin crystals, the total number of slip systems is 21 in the matrix/twin system. These slip systems in the matrix can be classified into three slip modes (see Tables 1 and 2 for the classification for the 12 slip systems in the matrix) depending on the orientations of the slip plane and the slip direction relative to the twin plane (the same definition as used in Refs. [31,33]). In the microstructural analysis dislocations belonging to the three slip modes are termed Mode I, Mode II and Mode III dislocations, respectively.

Slip Mode I: Both the slip plane and the slip direction are inclined to the TB, i.e. the ABC plane in Fig. 1. In this case, the slip planes include the planes BCD, CAD, and ABD in the matrix crystal and planes BCD_T, CAD_T and ABD_T, in the twin crystal. The slip directions are DB, DC, DA in the matrix crystal and D_TB, D_TC, D_TA in the twin crystal. The Burgers vectors (***b*** vectors) of dislocations corresponding to these slip systems are $\boldsymbol{b_{1M}}$, $\boldsymbol{b_{2M}}$, $\boldsymbol{b_{3M}}$, $\boldsymbol{b_{1T}}$, $\boldsymbol{b_{2T}}$ and $\boldsymbol{b_{3T}}$, as marked in Fig. 1.

Slip Mode II: The slip plane is inclined to the TB and the slip direction is parallel to the TB. In this case, the slip planes include the same sets of planes in the matrix and in the twin as in the Mode I case, but the slip directions are BC, CA and AB in both the matrix and the twin crystals. The Burgers vectors of dislocations corresponding to these slip systems are $\boldsymbol{b_4}$, $\boldsymbol{b_5}$ and $\boldsymbol{b_6}$, as marked in Fig. 1.

Slip Mode III: The slip plane and the slip direction are both parallel to the TB. These include the three slip systems shared by the matrix and the twin. The slip plane is the plane ABC and the slip directions are BC, CA, and AB in both the matrix and the twin crystals. The Burgers vectors of dislocations corresponding to these

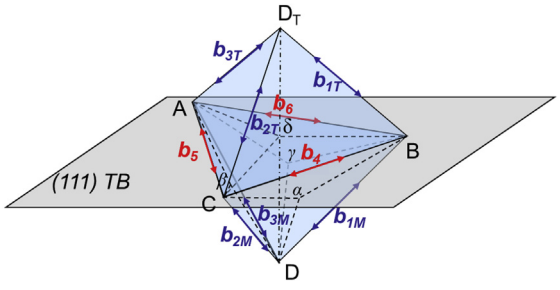

Fig. 1. A pair of Thompson tetrahedral of T/M crystals. The four vertices of the tetrahedron are labeled A, B, C and D, respectively. Symbols with subscript *T* represent objects in the twinned orientation. The hatched ACB plane is the twin plane. The upper and lower Thompson tetrahedra, i.e. ABCD and $ABCD_T$, illustrate the slip systems of matrix and twin crystals in the notation of Fig. 1, respectively. Each slip plane contains three slip directions <110>.

Table 1
Analysis of the values of $|\boldsymbol{g}\cdot\boldsymbol{b}|$ for perfect dislocations of <110> type Burgers vectors using three diffraction vectors in the $[01\bar{1}]$ zone axis of the matrix in a matrix/twin system. Here slip planes and Burgers vectors of dislocations are specific to Matrix. All Mode I dislocations are visible, while all Mode II/Mode III dislocations are invisible under $\boldsymbol{g_M} = 111$. Here, $\boldsymbol{b_5}$ is not identifiable.

Type	No.	Slip systems	Slip plane	Slip direction (Burgers vector)		$\lvert g\cdot b\rvert$ for different g_M		
						111_M	200_M	$\bar{1}11_M$
Mode I	1	$(1\bar{1}1)[011]$	BCD	DB ($\boldsymbol{b_{1M}}$)	1/2[011]	1	0	1
	2	$(1\bar{1}1)[110]$		DC ($\boldsymbol{b_{2M}}$)	1/2[110]	1	1	0
	3	$(\bar{1}11)[101]$	CAD	DA ($\boldsymbol{b_{3M}}$)	1/2[101]	1	1	0
	4	$(\bar{1}11)[110]$		DC ($\boldsymbol{b_{2M}}$)	1/2[110]	1	1	0
	5	$(11\bar{1})[101]$	ABD	DA ($\boldsymbol{b_{3M}}$)	1/2[101]	1	1	0
	6	$(11\bar{1})[011]$		DB ($\boldsymbol{b_{1M}}$)	1/2[011]	1	0	1
Mode II	7	$(1\bar{1}1)[\bar{1}01]$	BCD	BC ($\boldsymbol{b_4}$)	1/2$[\bar{1}01]$	0	1	1
	8	$(\bar{1}11)[01\bar{1}]$	CAD	CA ($\boldsymbol{b_5}$)	1/2$[01\bar{1}]$	0	0	0
	9	$(11\bar{1})[\bar{1}10]$	ABD	AB ($\boldsymbol{b_6}$)	1/2$[\bar{1}10]$	0	1	1
Mode III	10	$(111)[\bar{1}01]$	ABC	BC ($\boldsymbol{b_4}$)	1/2$[\bar{1}01]$	0	1	1
	11	$(111)[01\bar{1}]$	ABC	CA ($\boldsymbol{b_5}$)	1/2$[01\bar{1}]$	0	0	0
	12	$(111)[\bar{1}10]$	ABC	AB ($\boldsymbol{b_6}$)	1/2$[\bar{1}10]$	0	1	1

slip systems are also $\boldsymbol{b_4}$, $\boldsymbol{b_5}$, and $\boldsymbol{b_6}$, the same as in the case of Mode II.

The objective of the present study is to correlate the three compression directions (90°, 0° and 45° compressions) and the activation of the three modes of slip systems through analyzing the characteristics of the dislocation structure in deformed nt-Cu. To correlate the slip mode and the dislocation characteristics, a combined analysis of morphological features and Burgers vectors of observed dislocations has been applied. Because of the distinct geometrical relationships of the three modes of slip system with respect to the TBs, the dislocations generated from the three slip modes are expected to show different morphological features in the TEM images taken in the direction parallel to the twin plane [31]: (i) Mode I dislocations will pile up at the TBs and be transmitted across the boundary; (ii) Mode II dislocations are expected to move on inclined slip planes along the channel between the TBs. These dislocations may appear as threading dislocations spanning the lamellae; (iii) Mode III dislocations move along the TBs on slip planes parallel to TBs. They form steps on the TBs or they are seen as straight segments in the lamellae parallel to TBs. In previous studies of deformed Cu some of these features have been identified [31].

To determine the dislocation Burgers vectors, two-beam diffraction contrast experiments [44] were carried out in TEM based on the invisibility criterion $\boldsymbol{g}\cdot\boldsymbol{b} = 0$. In this study, six different $\boldsymbol{g}$ vectors ($\boldsymbol{g}$ vectors of matrix and twin crystals are labeled $\boldsymbol{g_M}$ and $\boldsymbol{g_T}$), $\boldsymbol{g_M} = 111$, $\boldsymbol{g_M} = 200$ and $\boldsymbol{g_M} = \bar{1}11$ for the matrix and $\boldsymbol{g_T} = 111$, $\boldsymbol{g_T} = 200$ and $\boldsymbol{g_T} = \bar{1}11$ for the twin were used, which belong to the common zone axis $[01\bar{1}]$ of the matrix and the twin, as shown in Fig. 2. For these three $\boldsymbol{g}$ vectors for the matrix, the values of $|\boldsymbol{g}\cdot\boldsymbol{b}|$ are shown in Table 1, here $\boldsymbol{b}$ indicate the six <011> type of Burgers vectors in a fcc crystal. Note that Table 1 shows only the analysis for the perfect dislocations in the matrix and the same analysis applies to the dislocations in the twin. Imaging the dislocations using these three $\boldsymbol{g}$ vectors shows the following features of visibility (taken the analysis of dislocations in the matrix as an example):

(1) Mode I dislocations ($\boldsymbol{b_{1M}}$, $\boldsymbol{b_{2M}}$, and $\boldsymbol{b_{3M}}$). With $\boldsymbol{g_M} = 111$, they are all visible, while the Mode II and Mode III dislocations $\boldsymbol{b_4}$, $\boldsymbol{b_5}$, $\boldsymbol{b_6}$ are all invisible, enabling separation of Mode I dislocations from More II and Mode III dislocations. A complete identification of $\boldsymbol{b_1}$ dislocations can be made by a combined use of the three diffraction vector, though it is not possible to distinguish between $\boldsymbol{b_{2M}}$ and $\boldsymbol{b_{3M}}$ dislocations.
(2) Mode II/Mode III dislocations ($\boldsymbol{b_4}$, $\boldsymbol{b_5}$ and $\boldsymbol{b_6}$). $\boldsymbol{b_4}$ and $\boldsymbol{b_6}$ with $\boldsymbol{g_M} = 111$ are invisible but visible simultaneously with $g_M = 200$ and $g_M = \bar{1}11$. This will allow identification of the observed dislocations under these conditions as Mode II or Mode III dislocations. Note that for the three $\boldsymbol{g}$ vectors used, $\boldsymbol{b_5}$ is invisible, which means that no dislocations with a Burgers vector of $\boldsymbol{b_5}$ were analyzed though they may be activated during the compression. However, this does not affect the analysis of the correlation between the loading direction and the slip modes. An unambiguous identification

Table 2
Geometrical relation of slip plane (SP) and slip direction (SD) with the twin plane (TP) in three slip modes, Modes I, II and III in the nt-Cu samples.

	Mode I		Mode II		Mode III	
	SP	SD	SP	SD	SP	SD
Inclined to TP	+	+	+			
Parallel to TP				+	+	+

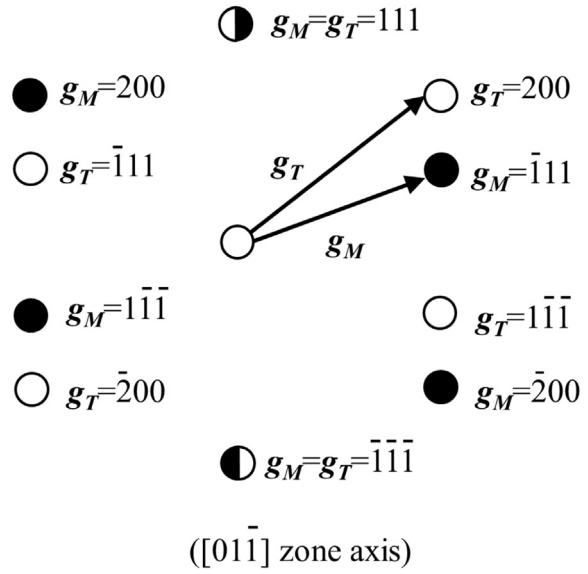

Fig. 2. The diffraction pattern of axis $[01\bar{1}]$, presenting the $\boldsymbol{g}$ vectors used to distinguish the Burgers vectors.

of Mode II and Mode III dislocations was achieved by taking also into account their morphological features with respect to the TBs, as described above.

Finally it should be pointed out that for pure Cu with stacking fault energy in the range of 40–78 mJ/m^2 [45–47], a perfect dislocation is expected to dissociate into two partial dislocations connected by a stacking fault, as revealed in previous studies of deformed Cu using the weak-bean dark-field (WBDF) techniques [48–50]. In the present study, the extended nature of the dislocations formed in the deformed nt-Cu was revealed by high resolution TEM observations (see Section 3.2). The activation and motion of partial dislocations along the TBs have been extensively observed in the nt-Cu deformed in 45° compression, which was reported in a previous study [31]. However, as the main objective of the present study is to analyze the correlation between the observed dislocations and the active slip systems under different loading directions, most of the analysis of dislocation Burgers vectors was done using two beam bright images at relatively low magnifications. In this case the morphology of an extended perfect dislocation formed in the lamellae presents like an un-extended perfect one, except a little wider and therefore the dislocations in the analysis were treated as perfect dislocations.

3. Results and discussion

3.1. Dislocation structures - 90° compression to 2% strain

Fig. 3a shows typical observations of dislocation structures from the 90° compressed nt-Cu sample with a strain of 2%, which was taken with $\boldsymbol{g}$ vector from $\boldsymbol{g_M} = \boldsymbol{g_T} = 111$ with a slight deviation, as otherwise the TBs will be totally invisible under a perfect $\boldsymbol{g_M} = \boldsymbol{g_T} = 111$ condition. The most striking feature in Fig. 3a is the observation of a set of long and roughly parallel dislocation lines (two of them are indicated by the black arrows 1 and 2) that transmit across tens of twin and matrix lamellae in a direction roughly perpendicular to the TBs. These dislocations revealed with $\boldsymbol{g_M} = \boldsymbol{g_T} = 111$ are identified as Mode I dislocations. Combining observations with other diffraction vectors (Fig. 3b, c, e and f) did not show the presence of other dislocation segments, suggesting that dislocations from slip modes II and III have not been activated.

Identification of Burgers vectors corresponding to the dislocation segments for dislocation line 1 and 2 shows interesting differences. For dislocation line 1, the segments in the matrix lamellae are visible in Fig. 3a and c but invisible in Fig. 3b, indicating that they have Burgers vector of $\boldsymbol{b_{1M}}$. Similar analysis of the segments of line 1 in the twin lamellae shows that they have a Burgers vector of $\boldsymbol{b_{2T}}$ or $\boldsymbol{b_{3T}}$. For dislocation line 2, the segments in the matrix are visible in Fig. 3a, b, but invisible in Fig. 3c indicating that they have a Burgers vector of $\boldsymbol{b_{2M}}$ or $\boldsymbol{b_{3M}}$. The segments of line 2 in the twin show a similar visibility to that of the matrix segments, meaning that they have a Burgers vector of $\boldsymbol{b_{2T}}$ or $\boldsymbol{b_{3T}}$.

Fig. 3d illustrates all the dislocation lines with different colors representing different Burgers vectors of dislocation segments in the matrix and the twin. When dislocation line 1 transmits across a TB, the Burgers vector would change from $\boldsymbol{b_{1M}}$ in the matrix to $\boldsymbol{b_{2T}}$/$\boldsymbol{b_{3T}}$ in the twin. For dislocation line 2, the Burgers vector $\boldsymbol{b_{2M}}$/$\boldsymbol{b_{3M}}$ in the matrix changes into $\boldsymbol{b_{2T}}$/$\boldsymbol{b_{3T}}$ in the twin. According to the dislocation lines in Fig. 3, there could be two possible transmissions of a dislocation: One is that the Burgers vector of dislocation segments in the matrix changes into a neighboring Burgers vector in the twin, such as from $\boldsymbol{b_{1M}}$ into $\boldsymbol{b_{2T}}$/$\boldsymbol{b_{3T}}$, $\boldsymbol{b_{2M}}$ into $\boldsymbol{b_{3T}}$, and $\boldsymbol{b_{3M}}$ into $\boldsymbol{b_{2T}}$. These changes are equivalent in geometry. The other possibility is that the Burgers vector in the matrix changes into its mirror Burgers vector in the twin, from $\boldsymbol{b_{2M}}$ into $\boldsymbol{b_{2T}}$ and from $\boldsymbol{b_{3M}}$ into $\boldsymbol{b_{3T}}$.

Such a process can be understood as a perfect Mode I dislocation DB in the matrix crystal is transmitted across a TB and producing a new Mode I dislocations in the twin, as shown in Fig. 4a. When a dislocation DB is transmitted across the TB and form a continuous dislocation line in the twin, its Burgers vector can change into AD_T, CD_T or BD_T in the twin crystal. The outcome may be two possible dislocation reactions, according to geometry. One reaction is into AD_T and CD_T, which are neighbors to the incoming dislocation DB and equivalent in geometry to DB. To implement the transformation of the Burgers vector, the corresponding dislocation reactions in Fig. 4a should be:

$$DB \rightarrow C\delta + AD_T \tag{1}$$

$$or \quad DB \rightarrow A\delta + CD_T \tag{2}$$

The other reaction is that the dislocation with $\boldsymbol{b}$ vector DB changes to a dislocation with a mirror $\boldsymbol{b}$ vector BD_T, and the corresponding dislocation reaction should be:

$$DB \rightarrow 2\delta D + BD_T \tag{3}$$

The energy barriers for these two kinds of reactions have been calculated by Zhu et al. [51]. The two reactions (1) and (2) are equivalent and the energy barrier is about 3.0 $\widehat{E}$+ 3.9$\tilde{E}$, $\widehat{E} = \frac{Ga^2}{72\pi(1-\nu)} \ln\frac{\sqrt{2}d}{a}$, $\tilde{E} = \frac{Ga^2}{72\pi(1-\nu)}$, where G is the shear modulus, ν is the Poisson's ratio, d is the grain size and a is the lattice parameter. This investigation indicated that this reaction gives the smallest energy barrier among all the dislocation reactions for a perfect dislocation to be fully or partly transmitted across the TB. The energy barrier of reaction (3) is about 4.5 $\widehat{E}$+ 7.5$\tilde{E}$, much higher than that of the reactions (1) and (2). Therefore, reaction (1) & (2) of Mode I have a preference. A Mode I dislocation can therefore continuously be transmitted across of TBs by repeating the same dislocation reactions.

Our observations have confirmed the occurrence of dislocation reactions (1) and (2) for dislocation/TB interactions under 90° compression, but cannot exclude the possibility of reaction (3), because $\boldsymbol{b_2}$ and $\boldsymbol{b_3}$ cannot be distinguished. For example, for dislocation line 2 in Fig. 3, the Burgers vector $\boldsymbol{b_{2M}}$ can change into $\boldsymbol{b_{3T}}$ or $\boldsymbol{b_{2T}}$ after transmission. But it may be advantageous that the Burgers vector in the twins changes from $\boldsymbol{b_{2M}}$ into $\boldsymbol{b_{3T}}$, considering the above analysis that indicates reaction (3) will hardly take place. This suggests that Mode I dislocations slightly changing their Burgers vector $\boldsymbol{b_M}$ into a neighboring Burgers vector in the twin $\boldsymbol{b_T}$ and transmit across TBs continuously by repeating the dislocation reactions (1) or (2).

Mode I dislocations have been observed by TEM [39,52] and by MD simulations [20,26]. The present observation indicates that reactions (1) and (2) appear to be the most probable interactions between dislocations and TBs at a low deformation strain. Such interactions will happen in grains with a low dislocation density, as pointed out by Ni et al. [52], consistent with the present observations that the long dislocation lines are observed only at a strain of 2%.

3.2. Dislocations structures - 90° compression to 6% strain

As the strain increased to 6%, almost no long dislocation lines were observed with $\boldsymbol{g_M} = \boldsymbol{g_T} = 111$ (Fig. 5a$_1$). The majority of TBs are still straight, visible and parallel to each other, but the TBs get blurred and widen. A large amount of dislocations are accumulated at the TBs and many dislocation segments are retained within the matrix and twin lamellae, similar to the observations in post-mortem images of deformed nt-Cu [14,15]. An image taken from

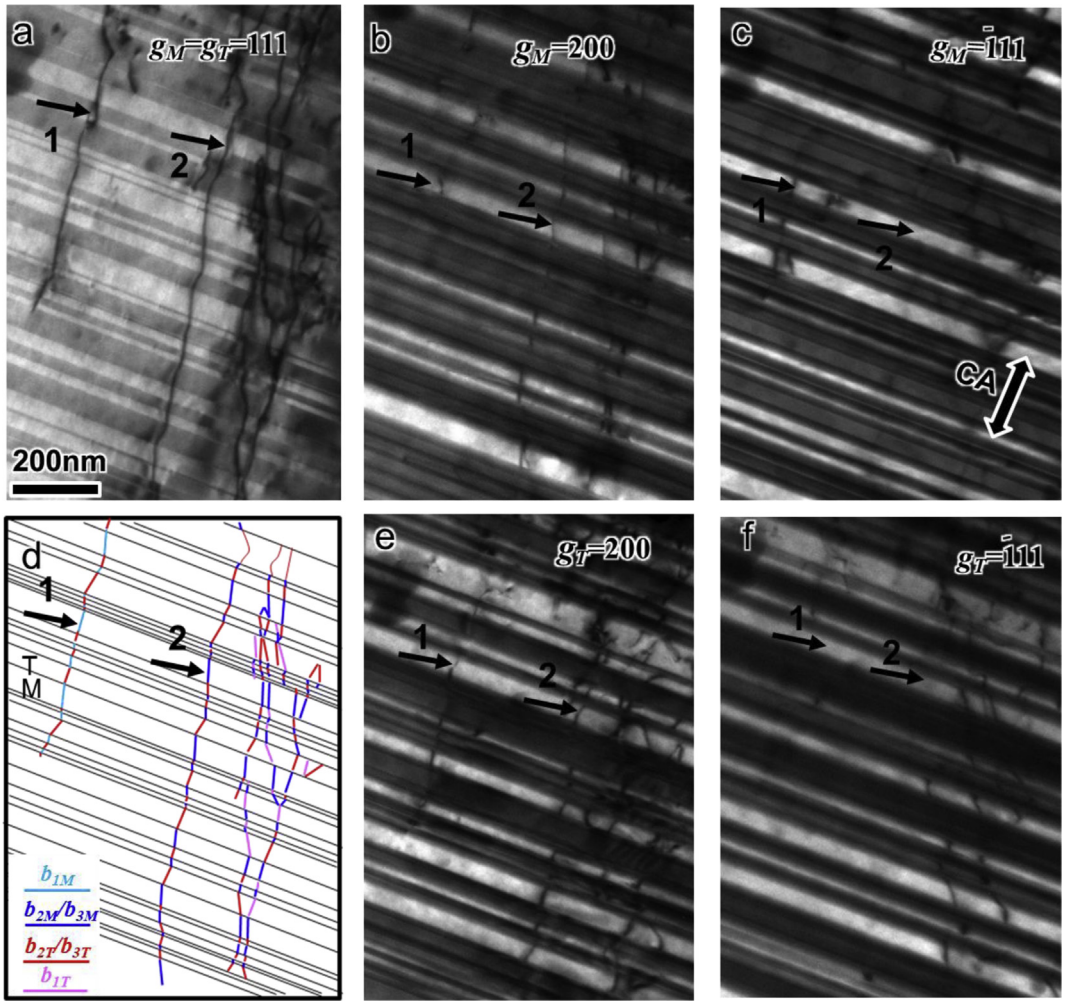

Fig. 3. Two-beam diffraction images of dislocations in 90° compressed nt-Cu with a strain of ~2%, under $g_M=g_T=111$ (a), $g_M=200$ (b), $g_M=\bar{1}11$ (c), $g_T=200$ (e) and $g_T=\bar{1}11$ (f), respectively. (d) Tracing of all the identified dislocation lines in (a, b, c, e and f), the different color distinguished the different ***b*** vectors of each dislocation segments. The black arrows 1 and 2 points to the long continuous Mode I dislocation lines with different ***b*** vector in matrixes and twins. The compressing axis (CA) direction is marked by a double arrow and "M" and "T" labeled out a pair of T/M lamellae, the same as below.(For interpretation of the references to colour in this figure legend, the reader is referred to the web version of this article.)

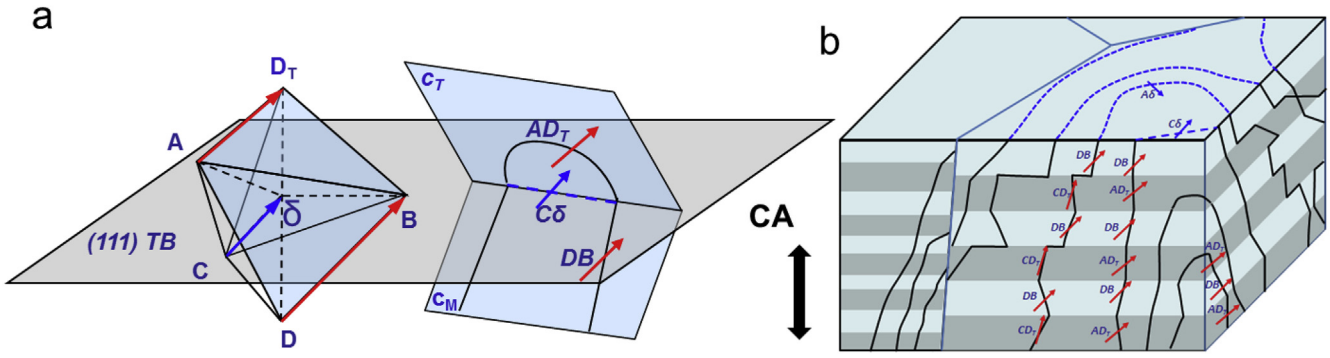

Fig. 4. Schematic illustration of Mode I dislocations interaction with TBs (a) and gliding in the columnar grains with parallel to TBs (b). The slip plane ABD and ABD_T are marked as c_M and c_T.

two-beam diffraction condition near $g_M = 200$ and $g_T = \bar{1}11$ is shown in Fig. 5b_1. An image taken from $g_M = \bar{1}11$ and $g_T = 200$ is shown in Fig. 5c_1. For clarity, Fig. 5a_2 to 5c_2 show the tracings of dislocations seen inside the lamellae in Fig. 5a_1 to 5c_1. It is evident that the dislocations seen in Fig. 5a_2 (both dislocation lines illustrated in red and blue) are a combination of dislocations seen in 5 b_2 (red lines) and Fig. 5 c_2 (blue lines). According to Table 1, the red lines are dislocations with Burgers vectors $\boldsymbol{b_{2M}/b_{3M}}$ & $\boldsymbol{b_{1T}}$, while blue lines are $\boldsymbol{b_{1M}}$. As for the dislocations on the TBs, no matter whether perfect or partial dislocations, they are all visible under

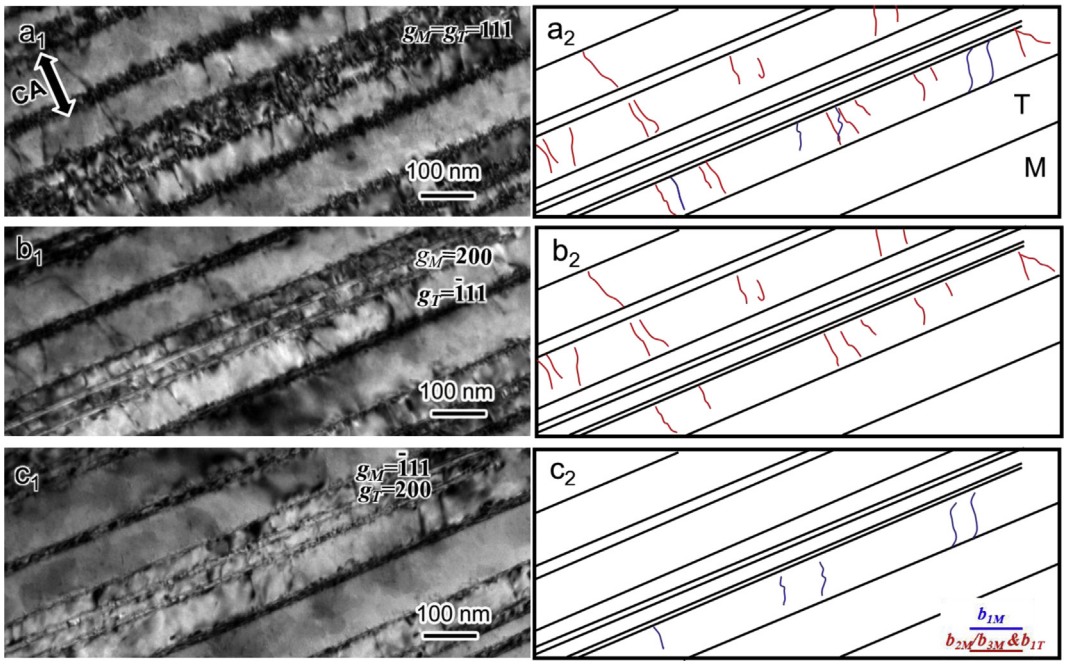

Fig. 5. Two-beam diffraction images of dislocations in the 90° compressed nt-Cu with a strain of ~6%, under $\boldsymbol{g_M}=\boldsymbol{g_T}=111$ (a_1), $\boldsymbol{g_M}=200$ and $\boldsymbol{g_T}=\bar{1}11$ (b_1), $\boldsymbol{g_M}=\bar{1}11$ and $\boldsymbol{g_T}=200$ (c_1). Tracings of the visible dislocations in a_1-c_1 are shown in (a_2-c_2) correspondingly.

$\boldsymbol{g_M} = \boldsymbol{g_T} = 111$ and classified as Mode I dislocations that with $\boldsymbol{b}$ vectors incline to the TBs and slipping towards the TB. The dislocations on the TBs and inside the lamellae are of the same type and dislocations with other Burgers vectors belonging to Mode II or Mode III were not observed.

Fig. 6 is a closer TEM observation of the dislocation structure in the vicinity of TBs and in the interior of twin lamellae. High resolution TEM images, Fig. 6b and c, show clearly that the dislocations are present in the form of extended dislocations associated with stacking faults. In Fig. 6b the stacking faults are connected with the TB indicating that the leading partials have been incorporated into the TB. It is also seen that the TB is significantly strained and has become defective due to the stored dislocations. Fig. 6c shows that each of the extended dislocations in a lamella is dissociated into two partial dislocations connected by a stacking fault with a width of about 2 nm. By drawing a Burgers circuit around an extended dislocation as shown in the inset of Fig. 6c, a vector corresponding to the closure failure of the Burgers circuit was determined to be equal to 1/4 [211], which is the projection of 1/2 [101] (DA in Fig. 1) on the $(01\bar{1})$ observation plane. Therefore, the 1/2 [101] extended dislocation is a 60° mixed dislocation. Similar Burgers circuit analyses were done for the two partials which generated closure failure vectors of 1/12 [211] and 1/6 [211], which correspond to the projected vectors on the $(01\bar{1})$ plane for a 30° Shockley partial βA (1/6 $[1\bar{1}2]$) and a 90° Shockley partial Dβ (1/6 [211]), respectively.

The continuous long dislocation lines formed at 2% spanning tens of twin lamellae in Fig. 3 are composed of short dislocation segments having different Burgers vectors in the twin and the matrix. The dislocation segments respectively in matrix and twin lamella will glide in different directions under the applied stress, as shown in Fig. 4b. Gradually, long individual dislocation lines will disintegrate into small dislocation segments distributed along the TBs. Furthermore, as the strain is increased, more and more Mode I dislocations are blocked and stored at TBs via dissociation reactions and dislocation/dislocation interactions.

3.3. Dislocations structures - 0° compression to 2% strain

Fig. 7a presents a typical TEM observation with $\boldsymbol{g_M} = \boldsymbol{g_T} = 111$ from the cross-section of nt-Cu sample deformed under 0° compression to a 2% strain. Several curved dislocation lines spanning several lamellae are observed, which shows a different morphology from the long straight dislocation lines observed in the case of 90° compression to the same strain (Fig. 3a). Fig. 7b, c, e and f show two-beam diffraction images using $\boldsymbol{g_M} = 200$, $\boldsymbol{g_M} = \bar{1}11$, $\boldsymbol{g_T} = 200$ and $\boldsymbol{g_T} = \bar{1}11$. The dislocation lines indicated by black arrow 1 are visible in Fig. 7a, c and 7e, which indicate that the segments forming dislocation line 1 in the matrix crystal have Burgers vectors of $\boldsymbol{b_{1M}}$ and the segments in the twin have Burger vectors of $\boldsymbol{b_{2T}}/\boldsymbol{b_{3T}}$. For dislocation line 2, it is visible in Fig. 7a, b and 7f but invisible in Fig. 7c and e, suggesting that Burgers vectors of $\boldsymbol{b_{2M}}/\boldsymbol{b_{3M}}$ for the line segments in the matrix crystal and $\boldsymbol{b_{1T}}$ for the segments in the twin.

Fig. 7d illustrates all dislocation lines with different colors representing different Burgers vectors. Both dislocation lines 1 and 2 belong to slip Mode I. The Burgers vectors of these dislocation lines change their directions slightly when crossing the TBs from $\boldsymbol{b_{1M}}$ to $\boldsymbol{b_{2T}}/\boldsymbol{b_{3T}}$ (or the reverse), similar to that observed in Fig. 3, but they present a different morphology, namely shorter and more curved than those seen in Fig. 3.

Besides the long dislocation lines, several tiny dislocation loops were also found near some TBs under $\boldsymbol{g}$ vectors of $\boldsymbol{g_T} = 200$ and $\boldsymbol{g_T} = \bar{1}11$, marked by green arrows in Fig. 7e and f. These dislocations were not revealed with $\boldsymbol{g_M} = \boldsymbol{g_T} = 111$ (Fig. 7a). According to the invisibility analysis (Table 1), these dislocation loops have the Burgers vectors of $\boldsymbol{b_4}$ or $\boldsymbol{b_6}$. Since these dislocation lines clearly are not parallel to the TB plane, they cannot be Mode III dislocations but must be Mode II dislocations.

3.4. Dislocations structures - 0° compression to 6% strain

Fig. 8 shows typical two-beam diffraction TEM images. The

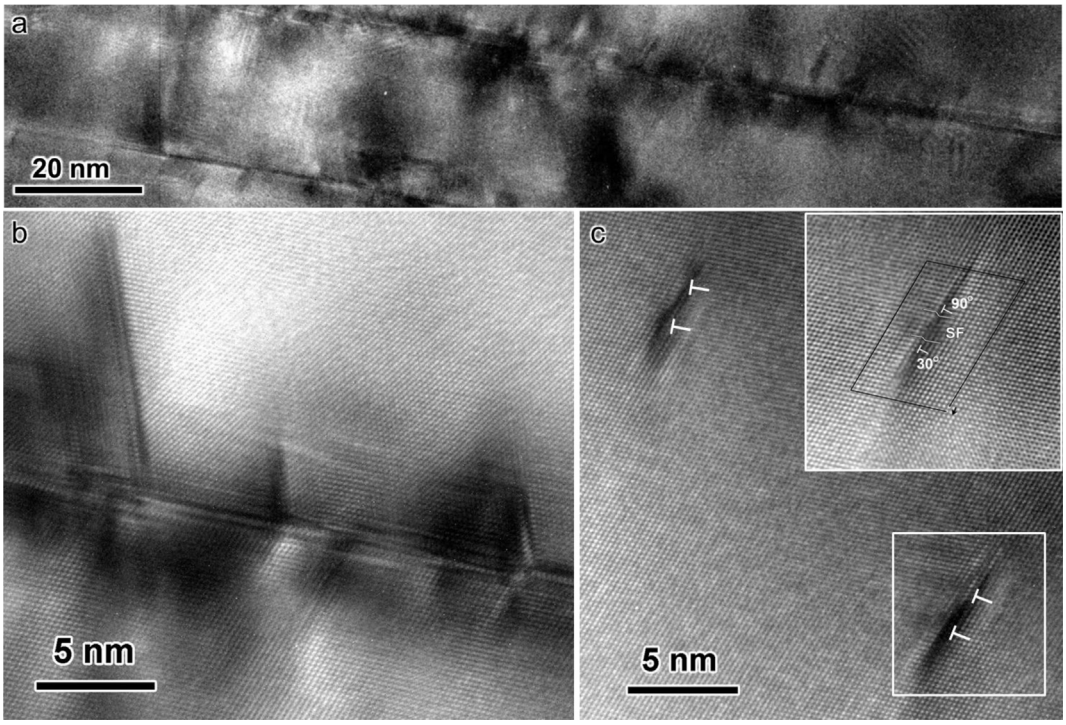

Fig. 6. TEM images showing the details of dislocation structures at the TBs and inside the lamellae of 90° compressed nt-Cu with a strain of ~6%, taken from $[01\bar{1}]$ axis. (a) The overall morphology of the TBs and dislocations in the observed region, (b) high resolution TEM image of dislocations at a TB and (c) high resolution TEM image of two extended dislocations in a lamella. Each of the extended dislocation is composed of two partials (marked as "⊥" in white) connected with a stacking fault. The identified types of the two partials are indicated in the inset in (c) which is a magnified inverse fast Fourier transformed high resolution TEM image of the area in the white square.

dislocations in the matrix lamellae marked by M_1, M_2 and M_3 are analyzed using $\boldsymbol{g_M} = \boldsymbol{g_T} = 111$, $\boldsymbol{g_M} = 200$ and $\boldsymbol{g_M} = \bar{1}11$ as shown in Fig. 8a_1- 8c_1. Most TBs are still straight. Observing from $\boldsymbol{g_M} = \boldsymbol{g_T} = 111$, Mode I dislocations are clearly seen both inside the twin lamellae and at the TBs. Comparing with Mode I dislocations observed in 90° compression (Fig. 5a), some are accumulated at the TBs but appears fewer than those in Fig. 5a. Some short dislocation segments are seen confined inside the matrix lamellae just like Fig. 5a. Fig. 8a_2–c_2 show the tracing of dislocations in the marked matrix lamellae in Fig. 8a_1–c_1. The dislocations illustrated by red and blue lines are all visible in Fig. 8a_1. The red dislocations are visible in Fig. 8b_1 but invisible in Fig. 8c_1, while the blue ones show the reverse occurrence, which indicates that both red and blue dislocations are Mode I dislocations but they have different Burgers vectors $\boldsymbol{b_{2M}}/\boldsymbol{b_{3M}}$ and $\boldsymbol{b_{1M}}$. However, the dislocations illustrated in the sketch by green lines are invisible in Fig. 8a_2, but visible in both Fig. 8b_2 and 8c_2. Similar to Fig. 7, these green dislocations belong to slip Mode II with Burgers vectors of $\boldsymbol{b_4}/\boldsymbol{b_6}$. It is worth noting that the observed Mode II dislocations (green) are very limited in number and present as short segments instead of continuous dislocation lines.

TEM observations in Figs. 7 and 8 indicate that both Modes I and II dislocations are active. Furthermore, it seems that Mode I dislocations also dominate the deformation of nt-Cu under 0° compression. However, from the previous study [31], active operation of Mode II slip systems, generating threading dislocations, is expected for 0° compression. To detect such threading dislocations, a sampling section inclined to the compression axis is more appropriate than a cross-section section that is parallel to the compression axis. A sample was therefore cut from a section 45° with respect to the compression axis (45° observation), as illustrated in Fig. 9.

Fig. 10a shows a two-beam diffraction image under $\boldsymbol{g_M} = 200$ of under 45° observation at 2% strain. TBs showed thickness fringes because the sample is tilted far away from the edge-on imaging condition, to see more details on the TBs and to observe the high density of Mode II dislocation tails along the TBs. Plenty of threading dislocation lines (indicated by black arrows) are spanning the twin lamellae with long tails on the TBs, quite different from the morphology in the cross-section section (Fig. 7b and e) under the same condition $\boldsymbol{g_M} = 200$ or $\boldsymbol{g_T} = 200$. The dislocations in Fig. 10 are all invisible when observing with $\boldsymbol{g_M} = \boldsymbol{g_T} = 111$, and they must belong to slip mode II with Burgers vectors of $\boldsymbol{b_4}$ or $\boldsymbol{b_6}$. The hairpin-like threading dislocation lines with long trailing tails, confined inside each twin lamella, makes them very easy to be identified, as illustrated in Fig. 9. Mode I dislocations are also observed (marked by white arrows in Fig. 10a), but much fewer in number than Mode II dislocations.

In the 6% compressed nt-Cu sample, large amount of dislocations from slip mode II were identified by their tails located on the TBs, from a cross sectional observations. As shown in Fig. 10b, many dislocation lines with a short head in the lamellae appeared under $\boldsymbol{g_M} = 200$. Different from the twinning partials (Mode III dislocations) on the TBs that may also visible under $\boldsymbol{g_M} = 200$, Mode II dislocation has an obvious dislocation head into the twin lamellae. The density of such dislocations increased significantly with increasing strain from 2% to 6%.

3.5. Dislocation structures - 45°compression to 6% strain

Fig. 11a and b shows the typical cross-sectional morphology of nt-Cu under 45° compression at 6% strain. Fig. 11a is viewed in the $[01\bar{1}]$ beam direction, which includes the $\boldsymbol{g}$ vectors of $\boldsymbol{g_M} = \boldsymbol{g_T} = 111$, $\boldsymbol{g_M} = 200$, $\boldsymbol{g_M} = \bar{1}11$, $\boldsymbol{g_T} = 200$ and $\boldsymbol{g_T} = \bar{1}11$, so that almost all possible dislocations from the three slip modes can be observed. According to the previous analysis, the dislocations types can be

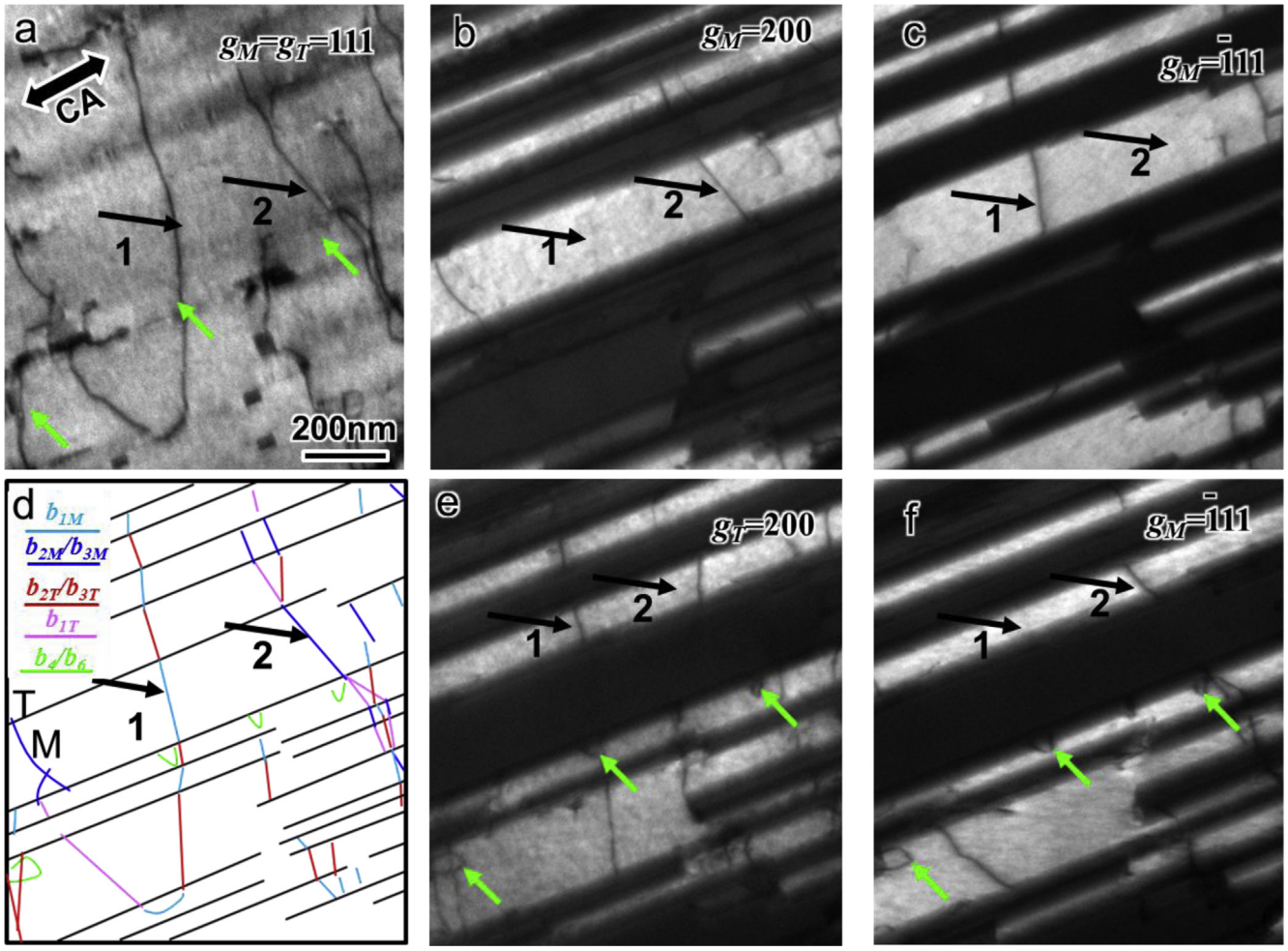

Fig. 7. Two-beam diffraction images of dislocations in the 0° compressed nt-Cu with a strain of ~2%, under $\boldsymbol{g_M}$=$\boldsymbol{g_T}$=111 (a), $\boldsymbol{g_M}$=200 (b), $\boldsymbol{g_M}$=$\bar{1}$11 (c), $\boldsymbol{g_T}$=200 (e) and $\boldsymbol{g_T}$=$\bar{1}$11 (f), respectively. (d) Tracing of all the identified dislocation lines in (a, b, c, e and f), the different color distinguished the different $\boldsymbol{b}$ vector of each dislocation segments. The black arrows 1 and 2 point to the long continuous Mode I dislocation lines with different $\boldsymbol{b}$ vectors in matrixes and twins. The green arrows point to the identified Mode II dislocations.(For interpretation of the references to colour in this figure legend, the reader is referred to the web version of this article.)

simply distinguished by their morphology. Dislocation lines cutting through the TBs (red arrows) are Mode I dislocations. Observing under two beam condition $\boldsymbol{g_M}$ = 200 (Fig. 11b), some dislocation lines with long tails appeared on the TBs (blue arrows), which is the typical morphology of Mode II dislocations, according to above analysis in Fig. 10. Besides the Mode I and Mode II dislocations, many dislocations (green arrows) with dislocation lines parallel to the TBs are observed inside the lamellae. These dislocations have slip planes parallel to the TBs and belong to slip Mode III. In the grains with coarse twin lamellae (Fig. 11c), plenty of Mode III dislocations are observed and their interactions with the Mode I and II dislocations are extensive.

3.6. Orientation, slip system and dislocation structure

The above observations clearly show that the active slip systems and dislocation configurations are strongly dependent on the loading direction in the highly oriented nt-Cu with an average twin thickness of 30 nm. This observation is in accord with previous studies of the relationship between the crystallography orientation and dislocation structures in deformed single crystals and polycrystalline metals [53–58]. In a recent study of nt-Cu with a twin thickness varying from a few nanometer to about 1 μm, it has been found that this relationship holds down to a twin thickness of 0.5 μm. In this fine structure, incidental dislocation boundaries (IDBs) and geometrically necessary boundaries (GNB) subdivided the volume between TBs, showing that the universal structural revolution can be extended from the micrometer length scale to 0.5 μm [59]. In this study, the characteristics of the deformation structure show that IDBs or cell boundaries and GNBs are not present in the fine structure, but there is a significant effect of loading direction on the dislocation structure showing a strong effect of the active slip systems. This observation is analyzed in the following by a Schmid factor analysis to predict active slip systems in the nt-Cu deformed in the three different loading directions.

Assuming the columnar nt-Cu has an ideal [111] out-of-plane texture, and the crystallographic orientation is randomly distributed in the deposition plane ($\boldsymbol{xy}$ plane). The loading direction of 90° compression is taken as the $\boldsymbol{z}$ axis of the sample coordinate system, i.e. the deposition direction, and the $\boldsymbol{x}$ direction as the direction of 0° compression (Fig. 12a). In order to express the in-plane orientation of the columnar grain relative to the imposed loading axis, the rotation angle $\boldsymbol{\theta}$ between the [01$\bar{1}$] orientation and the 0° compression ($\boldsymbol{x}$ axis) is taken to represent each single grain. The variation of the Schmid factors of the 12 slip systems as a function of $\boldsymbol{\theta}$, ranging from 0 to π in the three different compression experiments were calculated and are illustrated in Fig. 12b–d. In parallel, Table 3 lists the maximum values of Schmid factor for the

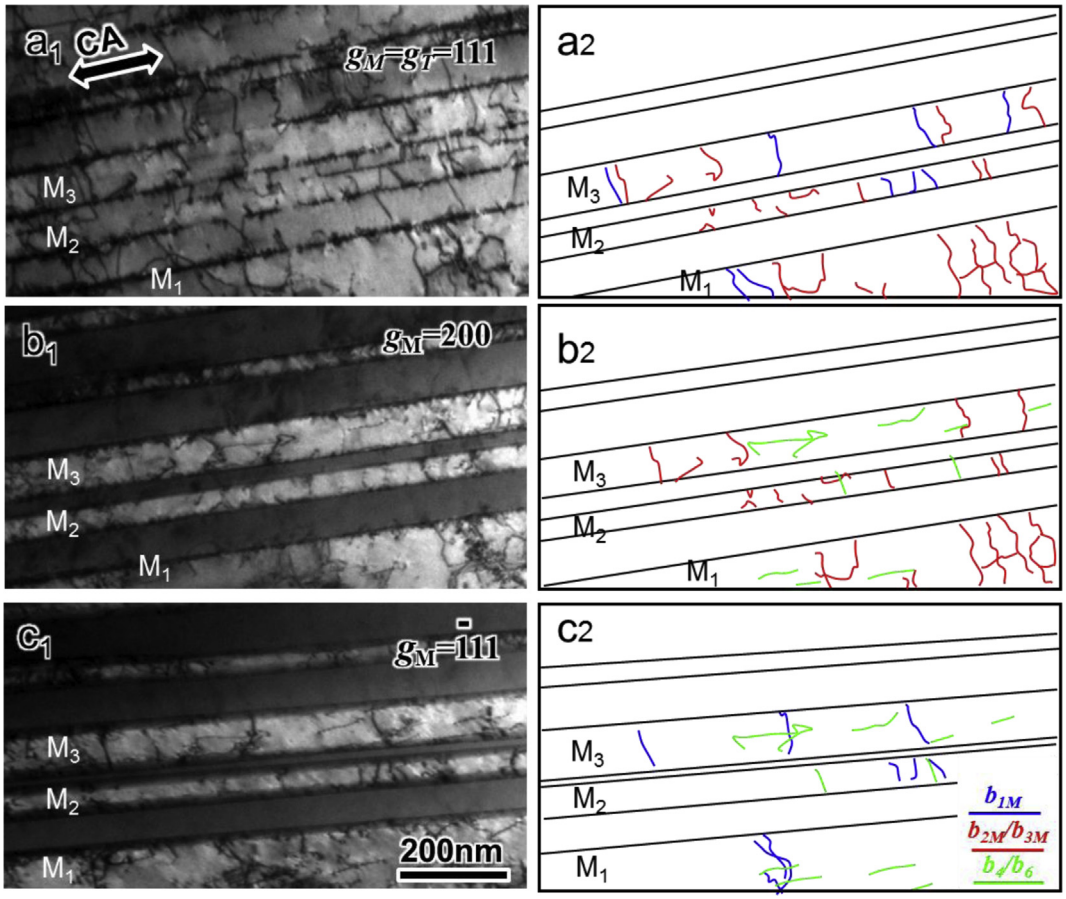

Fig. 8. Two-beam diffraction images of dislocations in 0° compressed nt-Cu with a strain of ~6%, under $g_M=g_T=111$ (a_1), $g_M=200$ (b_1), $g_M=\bar{1}11$ (c_1), respectively. Tracing of the visible dislocations in (a_1–c_1) are shown in (a_2–c_2) correspondingly.

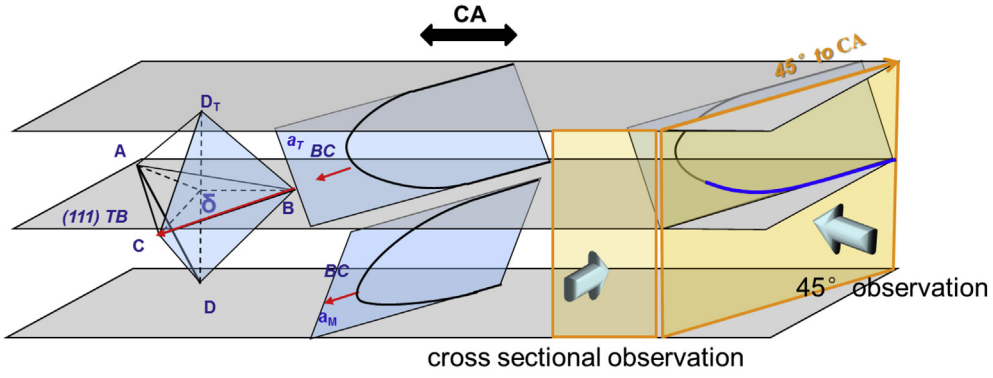

Fig. 9. Schematic illustration of Mode II dislocations interaction with TBs. The slip plane BCD and BCD_T are marked as a_M and a_T. The two observing plane that parallel and 45° to the compression axis of the 0° compressed samples were shown by two orange squares.(For interpretation of the references to colour in this figure legend, the reader is referred to the web version of this article.)

three slip modes under the three loading conditions.

For 90° compression, as shown in Fig. 12b, the six Mode I slip systems have a constant Schmid factors of 0.272. Schmid factors of all Mode II and Mode III slip systems are 0. This means that under 90° compression for grains with its (111) plane perfectly parallel to the TB, only Mode I dislocations are active and will dominate the plastic deformation, in accordance with the TEM observations shown in Figs. 3–6. In this case, the Schmid factor value of 0.272 is rather small compared with the maximum Schmid factors for the systems in 0° and 45° compression (Table 3). A relatively higher applied stress is thus required to activate the slip systems, resulting in a relatively higher yield and flow stress. This coincides with the compression results that a higher yield stress of 598 MPa was achieved in 90° compression, while yield stresses were only 463 MPa and 230 MPa for the 0° and 45° compression, respectively [31].

In Fig. 3 and 5, the Mode I dislocations are seen frequently and they bow out when meeting and transmitting across a TB. Mode I dislocations with Burgers vectors inclined to the TBs slip toward and transmit across the TBs. As visualized by reactions (1) and (2),

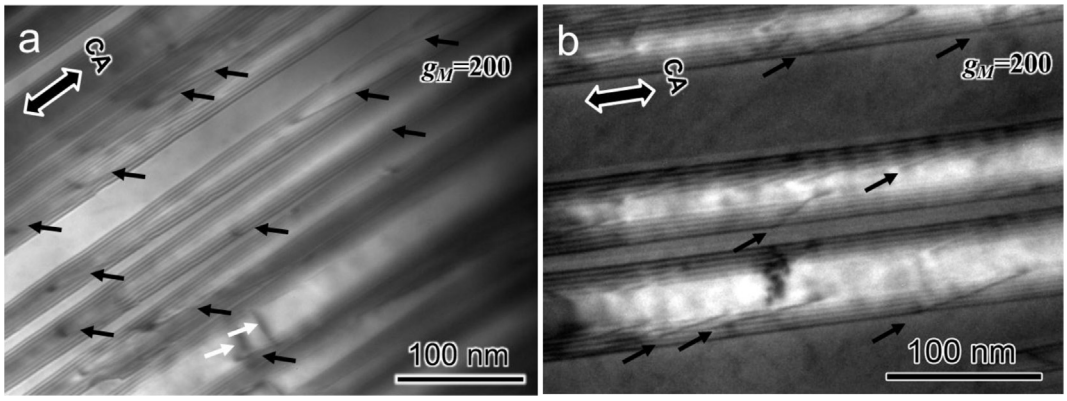

Fig. 10. Two-beam diffraction images of dislocations in nt-Cu under 0° compression under $\boldsymbol{g_M}$=200, (a) observed from the plane 45° to the compression axis at a strain of ~2% and (b) observed from cross sectional of threading dislocations at a strain of ~6%. Mode I dislocations are pointed by white arrows, and Mode II dislocations are pointed by black arrows.

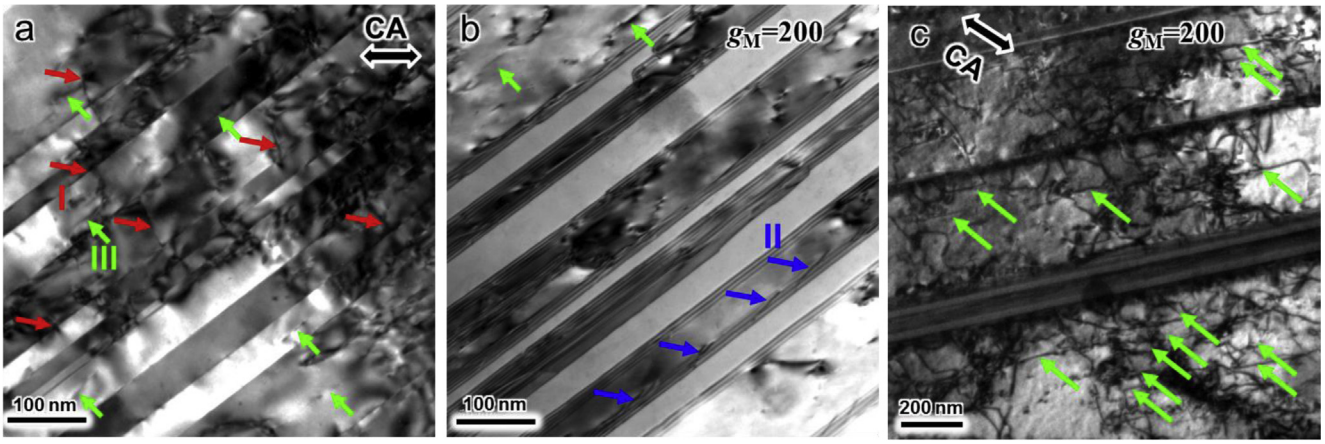

Fig. 11. TEM images of dislocations in the 45° compressed nt-Cu with a strain of ~6% from [01$\bar{1}$] axis (a), under $\boldsymbol{g_M}$=200 (b). Two-beam diffraction images the dislocations in a grain with coarse twin lamellae under $\boldsymbol{g_M}$=200 (c). The red, blue and grain arrows point out the Mode I, II and III dislocations, respectively.(For interpretation of the references to colour in this figure legend, the reader is referred to the web version of this article.)

the transmission of Mode I dislocation across TBs can produce partial dislocations at the TBs and many dislocations are retained in the lamellae between the TBs. These configurations will increase the flow stress in accordance with the Hall-Petch relationship and they may be the cause of the high work hardening rate observed at small strains.

For 0° compression, the largest Schmid factors (0.471) are associated with Mode II slip systems while the second largest Schmid factors (0.408) are related to Mode I slip systems (Fig. 12c and Table 3). For Mode III slip systems, the alignment of the loading axis parallel to TBs reduces their Schmid factors to zero at all θ angles. Therefore, in this case both Mode II and I slip systems are expected to be active. The combination of TEM observations from the cross-section and the 45° section verified the extensive activity of dislocations belonging to the Mode II and Mode I slip systems. However, observations of the dislocation structure in 0° compression show that Mode II dislocations are most active.

The dominance of Mode II dislocations in 0° compressions is further analyzed by comparing the activity of Mode I dislocations in the nt-Cu samples under 90° and 0° compressions to the same strain (6%), as shown in Fig. 13. The two images in Fig. 13 were taken under the same diffraction condition of $\boldsymbol{g_M} = \boldsymbol{g_T} = 111$. Apparently, Mode I dislocations under 0° compression (Fig. 13b) are much fewer than that under 90° compression (Fig. 13a). Mode II dislocations, which are gliding in the nanoscale lamellae are eventually stopped near obstacles such as grain boundaries and incoherent TB ledges, with a propagation direction parallel to TBs. The presence of high-density TBs cannot exert effective blockage to their movement; a slightly lower yield strength than 90° compression must be expected in agreement with [31]. Following propagation of dislocations between the TBs, dislocations will be stored at the interface (see Fig. 10) being a cause for the observed work hardening at small strains.

For 45° compression, the resolved shear stress is maximum on the TBs and the motion of Shockley partial dislocations along TBs in the fine twin lamellae region with thickness less than 100 nm and lead successively to detwinning (and as a result an apparent lateral migration of TBs) [31]. According to a Schmid factor calculation (Fig. 12d), Mode III slip systems have the maximum value 0.5 in 45 °compression, and perfect Mode III dislocations are also observed inside the twin lamellae (Fig. 11b) that have projected traces (line direction) parallel the TBs. Besides the twinning partials gliding on the TBs observed in the fine twin lamellae less than 100 nm [31], in the coarse lamellae with twin thicknesses more than 100 nm Mode III perfect dislocations are very active (Fig. 11c). Schmid factors of Mode II and Mode I slip systems vary with the angle θ. As shown in Table 3, the maximum Schmid factor of Mode I slip systems is 0.484, while it is 0.360 for Mode II. Different from the primary slip system which dominated deformation under 90° and 0° compressions, three slip modes are all active in many grains in 45° compression.

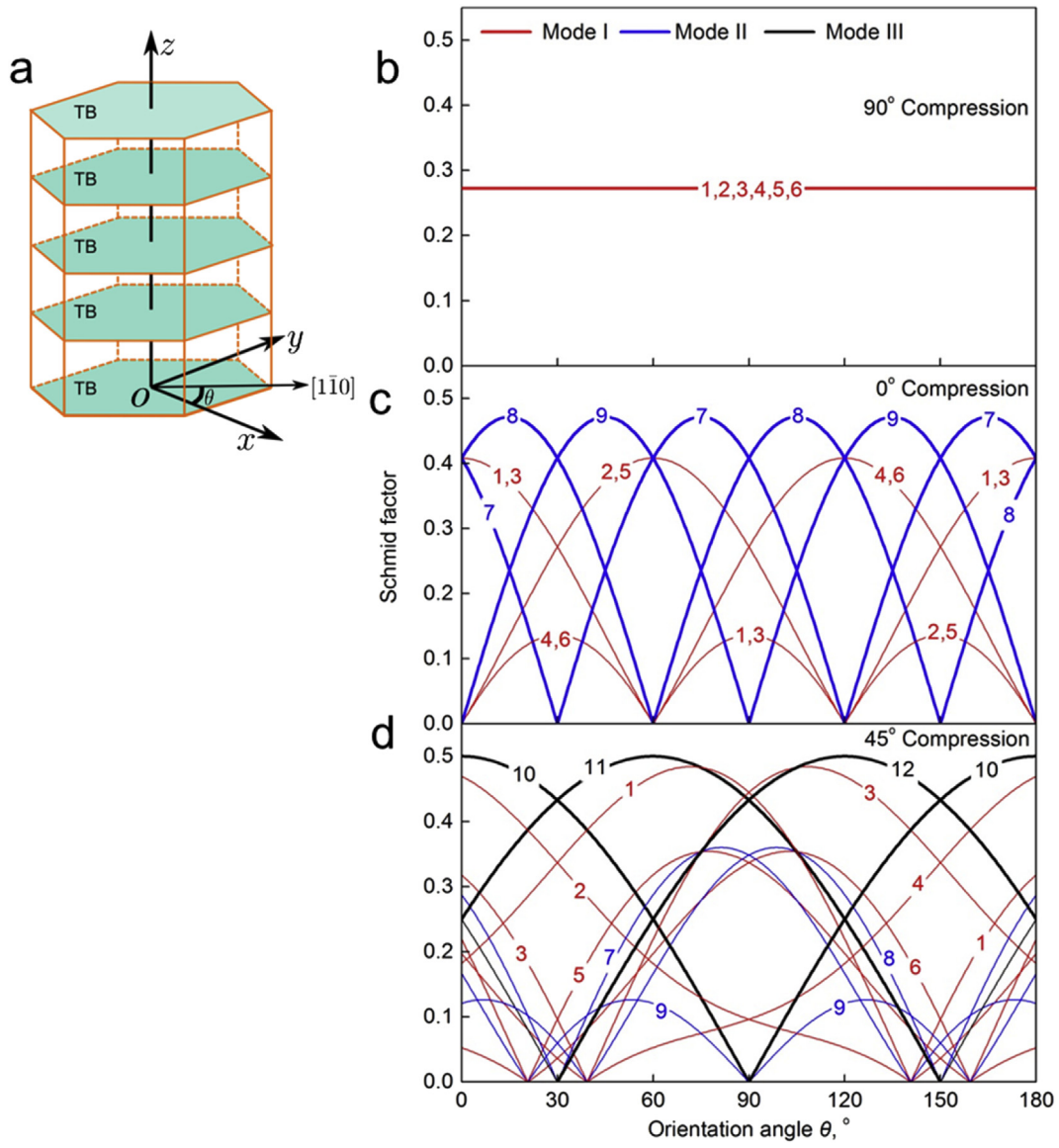

Fig. 12. (a) Illustration of loading direction with respect to TBs. The ***z*** axis is the 90° compression direction, the ***x*** axis is 0° compression direction, and θ is the angle between [1$\bar{1}$0] direction in the twin plane and the loading axis. Variation in Schmid factors of 12 slip systems (as listed in Table 1) as a function of angel θ for 90° (b), 0° (c) and 45° (d) compression.

Table 3
Maximum Schmid factors of three slip Modes under different compression directions of the nt-Cu sample.

Slip system type	Maximum Schmid factors		
	90° compression	0° compression	45° compression
Mode I	0.272	0.408	0.484
Mode II	0	0.471	0.360
Mode III	0	0	0.5

As a result, the interactions among three types of dislocations can take place, especially in the coarse lamellae with a thickness of more than 100 nm (Fig. 11a and c). The high density of partial dislocations along TBs and the interaction of dislocations from three slip modes will lead to significant work hardening, extending to 10% strain as observed previously [31]. However besides the various dislocation structures and the interactions between dislocations and TBs discussed above, the possible formation of other dislocation debris like Lomer-Cottrell locks and stacking fault tetrahedra [60–62] may also have a role to play in determining the mechanical response, which is for future research.

4. Conclusions

Nanotwinned Cu with an average twin thickness of 30 nm has been deformed to strains of 2% and 6% by compression in three directions to study the correlations between slip patterns and dislocation structures examined by TEM. The conclusions are the following.

In accord with polycrystalline plasticity modeling a $\boldsymbol{g}\cdot\boldsymbol{b}$ analysis of dislocations has shown a clear correlation between the load direction and the slip mode. (i) In 90° compression, Mode I dislocations are identified. (ii) In 0° compression, Mode I and Mode II dislocations are present with dominance of Mode II dislocations. (iii) In 45° compression, dislocations from all three slip modes are found.

The interaction of dislocations with the TBs varies with the compression direction. (i) In 90° compression, dislocations

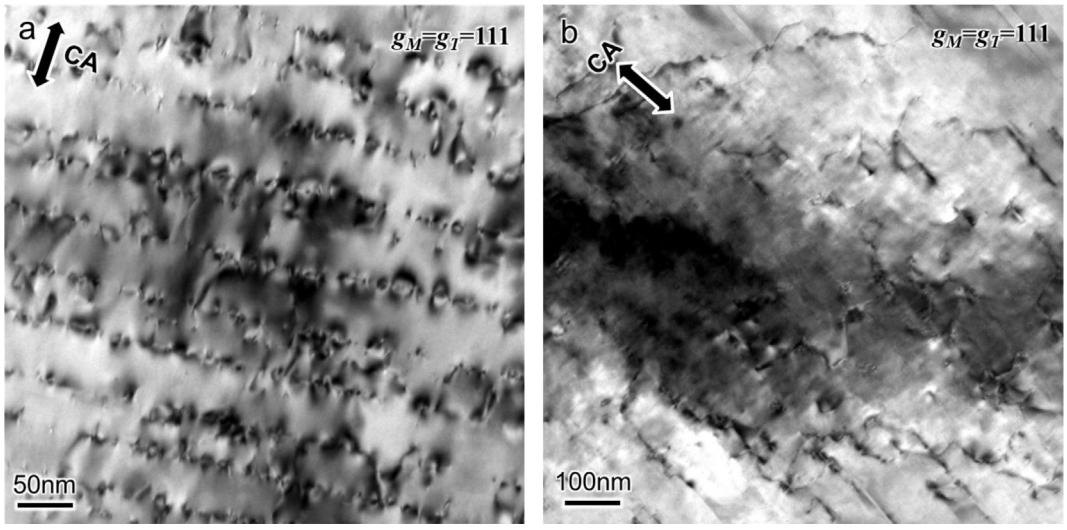

Fig. 13. Two-beam diffraction images of dislocations in nt-Cu 90° compressed (a) and 0° compressed (b) samples with a strain of ~6%, under $g_M=g_T=111$.

transmit across multiple TBs at low strain and accumulate at TBs at large strain. (ii) In 0° compression, threading dislocations inside the T/M lamellae are confined by the TBs with long dislocation tails at the boundaries. (iii) In 45° compression, dislocation interactions and dislocation tangling in the T/M lamellae are pronounced.

The structural evolution in nt-Cu documents a strong correlation between orientation, active slip systems and dislocation structures. This is in accord with previous findings for deformed single crystals and polycrystals extending this correlation over multiple length scales.

Acknowledgments

This research was supported by the National Basic Research Program of China (973 Program, 2012CB932202), National Natural Science Foundation of China (Nos. 51420105001, 51371171 and 51101163) and Key Research Program of Frontier Sciences, CAS. The authors acknowledge the Danish National Research Foundation (Grant No DNRF86-5) and Natural Science Foundation of China (Grant No. 51261130091) for supporting the Danish-Chinese Center for Nanometals, within which part of the present work was performed.

References

[1] L. Lu, Y.F. Shen, X.H. Chen, L.H. Qian, K. Lu, Ultrahigh strength and high electrical conductivity in copper, Science 304 (2004) 422–426.
[2] K. Lu, L. Lu, S. Suresh, Strengthening materials by engineering coherent internal boundaries at the nanoscale, Science 324 (2009) 349–352.
[3] L. Lu, X. Chen, X. Huang, K. Lu, Revealing the maximum strength in nanotwinned copper, Science 323 (2009) 607–610.
[4] X. Zhang, H. Wang, X.H. Chen, L. Lu, K. Lu, R.G. Hoagland, A. Misra, High-strength sputter-deposited Cu foils with preferred orientation of nanoscale growth twins, Appl. Phys. Lett. 88 (2006) 173116.
[5] X. Zhang, A. Misra, H. Wang, T.D. Shen, M. Nastasi, T.E. Mitchell, J.P. Hirth, R.G. Hoagland, J.D. Embury, Enhanced ardening in Cu/330 stainless steel multilayers by nanoscale twinning, Acta Mater. 52 (2004) 995–1002.
[6] E. Ma, Y.M. Wang, Q.H. Lu, M.L. Sui, L. Lu, K. Lu, Strain hardening and large tensile elongation in ultrahigh-strength nano-twinned copper, Appl. Phys. Lett. 85 (2004) 4932–4934.
[7] X.H. Chen, L. Lu, K. Lu, Electrical resistivity of ultrafine-grained copper with nanoscale growth twins, J. Appl. Phys. 102 (2007).
[8] A. Stukowski, K. Albe, D. Farkas, Nanotwinned fcc metals: strengthening versus softening mechanisms, Phys. Rev. B 82 (2010).
[9] A. Singh, L. Tang, M. Dao, L. Lu, S. Suresh, Fracture toughness and fatigue crack growth characteristics of nanotwinned copper, Acta Mater. 59 (2011) 2437–2446.
[10] Q.S. Pan, Q.H. Lu, L. Lu, Fatigue behavior of columnar-grained Cu with preferentially oriented nanoscale twins, Acta Mater. 61 (2013) 1383–1393.
[11] Q.S. Pan, L. Lu, Strain-controlled cyclic stability and properties of Cu with highly oriented nanoscale twins, Acta Mater. 81 (2014) 248–257.
[12] X. Li, M. Dao, C. Eberl, A.M. Hodge, H. Gao, Fracture, fatigue, and creep of nanotwinned metals, MRS Bull. 41 (2016) 298–304.
[13] T. Zhu, H.J. Gao, Plastic deformation mechanism in nanotwinned metals: an insight from molecular dynamics and mechanistic modeling, Scr. Mater. 66 (2012) 843–848.
[14] X.H. Chen, L. Lu, Work hardening of ultrafine-grained copper with nanoscale twins, Scr. Mater. 57 (2007) 133–136.
[15] Y.F. Shen, L. Lu, Q.H. Lu, Z.H. Jin, K. Lu, Tensile properties of copper with nanoscale twins, Scr. Mater. 52 (2005) 989–994.
[16] A.M. Hodge, Y.M. Wang, T.W. Barbee Jr., Mechanical deformation of high-purity sputter-deposited nano-twinned copper, Scr. Mater. 59 (2008) 163–166.
[17] N. Li, J. Wang, S. Mao, H. Wang, In situ nanomechanical testing of twinned metals in a transmission electron microscope, MRS Bull. 41 (2016) 305–313.
[18] X.Y. Li, Y.J. Wei, L. Lu, K. Lu, H.J. Gao, Dislocation nucleation governed softening and maximum strength in nano-twinned metals, Nature 464 (2010) 877–880.
[19] L. Zhu, H. Ruan, X. Li, M. Dao, H. Gao, J. Lu, Modeling grain size dependent optimal twin spacing for achieving ultimate high strength and related high ductility in nanotwinned metals, Acta Mater. 59 (2011) 5544–5557.
[20] Z.X. Wu, Y.W. Zhang, D.J. Srolovitz, Dislocation-twin interaction mechanisms for ultrahigh strength and ductility in nanotwinned metals, Acta Mater. 57 (2009) 4508–4518.
[21] Q. Lu, M. Sui, X. Huang, D. Li, N. Hansen, Length scale effect on the deformation microstructures of grown-in twins in copper, Philos. Mag. 94 (2014) 2262–2280.
[22] Y.M. Wang, F. Sansoz, T. LaGrange, R.T. Ott, J. Marian, T.W. Barbee Jr., A.V. Hamza, Defective twin boundaries in nanotwinned metals, Nat. Mater. 12 (2013) 697–702.
[23] N. Li, J. Wang, J.Y. Huang, A. Misra, X. Zhang, Influence of slip transmission on the migration of incoherent twin boundaries in epitaxial nanotwinned Cu, Scr. Mater. 64 (2011) 149–152.
[24] M. Chassagne, M. Legros, D. Rodney, Atomic-scale simulation of screw dislocation/coherent twin boundary interaction in Al, Au, Cu and Ni, Acta Mater. 59 (2011) 1456–1463.
[25] N. Lu, K. Du, L. Lu, H.Q. Ye, Transition of dislocation nucleation induced by local stress concentration in nanotwinned copper, Nat. Commun. 6 (2015) 7648.
[26] Z.H. Jin, P. Gumbsch, K. Albe, E. Ma, K. Lu, H. Gleiter, H. Hahn, Interactions between non-screw lattice dislocations and coherent twin boundaries in face-centered cubic metals, Acta Mater. 56 (2008) 1126–1135.
[27] Z.H. Jin, P. Gumbsch, E. Ma, K. Albe, K. Lu, H. Hahn, H. Gleiter, The interaction mechanism of screw dislocations with coherent twin boundaries in different face-centred cubic metals, Scr. Mater. 54 (2006) 1163–1168.
[28] P. Gu, M. Dao, S. Suresh, Analysis of size-dependent slip transfer and inter-twin flow stress in a nanotwinned fcc metal, Acta Mater. 67 (2014) 409–417.
[29] Z.X. Wu, Y.W. Zhang, D.J. Srolovitz, Deformation mechanisms, length scales and optimizing the mechanical properties of nanotwinned metals, Acta Mater. 59 (2011) 6890–6900.
[30] H. Zhou, X. Li, S. Qu, W. Yang, H. Gao, A jogged dislocation governed strengthening mechanism in nanotwinned metals, Nano Lett. 14 (2014) 5075–5080.
[31] Z.S. You, X.Y. Li, L.J. Gui, Q.H. Lu, T. Zhu, H.J. Gao, L. Lu, Plastic anisotropy and associated deformation mechanisms in nanotwinned metals, Acta Mater. 61

(2013) 217–227.
[32] Z.S. You, L. Lu, K. Lu, Tensile behavior of columnar grained Cu with preferentially oriented nanoscale twins, Acta Mater. 59 (2011) 6927–6937.
[33] T. Zhu, H. Gao, Plastic deformation mechanism in nanotwinned metals: an insight from molecular dynamics and mechanistic modeling, Scr. Mater. 66 (2012) 843–848.
[34] V. Borovikov, M.I. Mendelev, A.H. King, R. LeSar, Effects of Schmid factor and slip nucleation on deformation mechanism in columnar-grained nanotwinned Ag and Cu, J. Appl. Phys. 117 (2015) 85302.
[35] Y.B. Wang, M.L. Sui, E. Ma, In situ observation of twin boundary migration in copper with nanoscale twins during tensile deformation, Philos. Mag. Lett. 87 (2007) 935–942.
[36] J. Wang, N. Li, O. Anderoglu, X. Zhang, A. Misra, J.Y. Huang, J.P. Hirth, Detwinning mechanisms for growth twins in face-centered cubic metals, Acta Mater. 58 (2010) 2262–2270.
[37] N. Li, J. Wang, A. Misra, X. Zhang, J.Y. Huang, J.P. Hirth, Twinning dislocation multiplication at a coherent twin boundary, Acta Mater. 59 (2011) 5989–5996.
[38] C.J. Shute, B.D. Myers, S. Xie, S.Y. Li, T.W. Barbee Jr., A.M. Hodge, J.R. Weertman, Detwinning, damage and crack initiation during cyclic loading of Cu samples containing aligned nanotwins, Acta Mater. 59 (2011) 4569–4577.
[39] Y.B. Wang, M.L. Sui, Atomic-scale in situ observation of lattice dislocations passing through twin boundaries, Appl. Phys. Lett. 94 (2009) 021909.
[40] Y.B. Wang, B. Wu, M.L. Sui, Dynamical dislocation emission processes from twin boundaries, Appl. Phys. Lett. 93 (2008) 041906.
[41] N. Li, J. Wang, X. Zhang, A. Misra, In-situ TEM study of dislocation-twin boundaries interaction in nanotwinned Cu films, Jom 63 (2011) 62–65.
[42] N. Lu, K. Du, L. Lu, H.Q. Ye, Transition of dislocation nucleation induced by local stress concentration in nanotwinned copper, Nat. Commun. 6 (2015) 7648.
[43] S.R. Kalidindi, C.A. Bronkhorst, L. Anand, Crystallographic texture evolution in bulk deformation processing of fcc metals, J. Mech. Phys. Solids 40 (1992) 537–569.
[44] C.B.C. David, B. Williams, Transmission Electron Microscopy, Springer US, 2009.
[45] W.M. Stobbs, C.H. Sworn, Weak beam technique as applied to determination of Stacking-fault energy of copper, Philos. Mag. 24 (1971) 1365–1381.
[46] D.J. Cockayne, M.L. Jenkins, I.L.F. Ray, Measurement of stacking-fault energies of pure face-centred cubic metals, Philos. Mag. 24 (1971) 1383–1392.
[47] L. Murr, Interfacial Phenomena in Metals and Alloys, Addison-Wesley, 1975.
[48] M. Niewczas, Transmission electron microscopy observations of debris structure in deformed copper single crystals, Philos. Mag. *A* 82 (2002) 393–414.
[49] A.N. Stroh, The strength of lomer-cottrell sessile dislocations, Philos. Mag. 1 (1956) 489–502.
[50] M.H. Loretto, Lm Clarebro, R.L. Segall, Stacking-fault tetrahedrain deformed face-centred cubic metals, Philos. Mag. 11 (1965) 459–465.
[51] Y.T. Zhu, X.L. Wu, X.Z. Liao, J. Narayan, L.J. Kecskes, S.N. Mathaudhu, Dislocation-twin interactions in nanocrystalline fcc metals, Acta Mater. 59 (2011) 812–821.
[52] S. Ni, Y.B. Wang, X.Z. Liao, R.B. Figueiredo, H.Q. Li, S.P. Ringer, T.G. Langdon, Y.T. Zhu, The effect of dislocation density on the interactions between dislocations and twin boundaries in nanocrystalline materials, Acta Mater. 60 (2012) 3181–3189.
[53] X. Huang, G. Winther, Dislocation structures. Part I. Grain orientation dependence, Philos. Mag. 87 (2007) 5189–5214.
[54] G. Winther, X. Huang, Dislocation structures. Part II. Slip system dependence, Philos. Mag. 87 (2007) 5215–5235.
[55] G.M. Le, A. Godfrey, C.S. Hong, X. Huang, G. Winther, Orientation dependence of the deformation microstructure in compressed aluminum, Scr. Mater. 66 (2012) 359–362.
[56] F.X. Lin, A. Godfrey, G. Winther, Grain orientation dependence of extended planar dislocation boundaries in rolled aluminium, Scr. Mater. 61 (2009) 237–240.
[57] Q. Liu, D.J. Jensen, N. Hansen, Effect of grain orientation on deformation structure in cold-rolled polycrystalline aluminium, Acta Mater. 46 (1998) 5819–5838.
[58] N. Hansen, X. Huang, W. Pantleon, G. Winther, Grain orientation and dislocation patterns, Philos. Mag. 86 (2006) 3981–3994.
[59] G.M. Le, A. Godfrey, N. Hansen, W. Liu, G. Winther, X. Huang, Influence of grain size in the near-micrometre regime on the deformation microstructure in aluminium, Acta Mater. 61 (2013) 7072–7086.
[60] M. Niewczas, Z.S. Basinski, S.J. Basinski, J.D. Embury, Deformation of copper single crystals to large strains at 4.2 K - I. Mechanical response and electrical resistivity, Philos. Mag. *A* 81 (2001) 1121–1142.
[61] S. Kojima, S.J. Zinkle, H.L. Heinisch, Radiation hardening in neutron-irradiated polycrystalline copper: barrier strength of defect clusters, J. Nucl. Mater. 179 (1991) 982–985.
[62] K.Y. Yu, D. Bufford, C. Sun, Y. Liu, H. Wang, M.A. Kirk, M. Li, X. Zhang, Removal of stacking-fault tetrahedra by twin boundaries in nanotwinned metals, Nat. Commun. 4 (2013) 1377.